An investigation of the active tectonics in central-eastern mainland Greece with imaging and decomposition of topographic and aeromagnetic data

Andreas Tzanis [a,*], Haralambos Kranis [b], Stylianos Chailas [a]

[a] Department of Geophysics – Geothermy, University of Athens, Panepistimiopoli, 15784 Zografou, Greece
[b] Department of Dynamic and Applied Geology, University of Athens, Panepistimiopoli, 15784 Zografou, Greece

ARTICLE INFO

ABSTRACT

We report the results of a joint analysis of aeromagnetic, topographic and tectonic data in central-eastern mainland Greece. The emphasis of the analysis is placed on the detection of coherent lineations (discontinuities), collocated and correlated with faulting structures detected by geological field observation. To this effect, edge detection and image enhancement were applied to digital aeromagnetic anomaly maps and digital elevation models, comprising bidirectional differentiation, wavelet transformation (imaging) and spatial decomposition/reconstruction in the wavenumber domain. The analysis facilitated the detection of significant topographic lineaments with NNE–SSW, ENE–WSW and ESE–WNW orientations. Respectively, the aeromagnetic data exhibit two families of significant NE–SW, and one family of ESE–WNW lineaments. The major aeromagnetic and topographic lineaments coincide and have comparable width scales of the order of 2–3 km, indicating that they are produced by significant discontinuities in the upper crust. The kinematics of the NE–SW faults varies between oblique-slip and strike-slip. These faults affect Neogene to Late Quaternary deposits and have been responsible for the formation of transverse depressions and horsts. This is also corroborated by focal plane solutions from small earthquakes recorded by local networks. The nature of these structures is not yet clear. However, they have been detected by diverse methodologies, they have considerable extent and are apparently active. These attributes suggest that they may possibly be related to the propagation and diffusion of the North Anatolian and North Aegean fault systems into the Greek mainland.

© 2009 Elsevier Ltd. All rights reserved.

1. Introduction

It is a piece of trivial knowledge, that tectonic activity imprints the surface of the earth with discontinuities detectable by direct observation and/or by the analysis of digital elevation models or aerial and satellite images. It is also common, more or less, knowledge that the total intensity magnetic anomaly maps capture the static distribution of geological units that contain ferromagnetic minerals and are permanently or inductively magnetized in the Earth's main magnetic field. This distribution can be determined with conventional analysis methods designed to extract the geometry and magnetic properties of the structures producing the anomalies.

Tectonic activity may also imprint magnetized geological bodies with analogous discontinuities, detectable with similar analysis methods. This is possible because faulting processes will rupture such formations and dislocate the dissected blocks, "shearing" the local field and producing lateral gradients in the total field intensity. Moreover, they initiate secondary processes that destroy the magnetic susceptibility and remanent magnetization by creating secondary permeability that allows water to infiltrate and chemically alter the fragmented material in and around fault zones. Notably, when fault slip (dislocation) is small, the latter mechanism is more prominent, producing elongate "ridges" and "valleys" in the total intensity map. The location of the fault would, then, be indicated by the "valley" structures. Finally, the interfaces between magnetic and non-magnetic geological formations brought together by tectonic movements are evident by abrupt lateral changes in the intensity of the magnetic field. To summarize, tectonic processes might result in elongate discontinuities (lineaments) in the static magnetic field, which should be collocated and correlated with fault scarps detectable by the analysis of digital topographic models and direct field observations. It is thus possible to use aeromagnetic data as a tool of locating traces of buried faulting structures.

Herein, we apply these ideas to the study of central-eastern mainland Greece, in the hope of deriving further insights and constraints on the active tectonic modes of the study area. Active tectonics, particularly when it is complex, shapes the topographic

and magnetic landscapes over a broad range of scales, from the local to the regional. For instance, the surface expression of a fault or fault zone, which may change rapidly with respect to position, can be a local scale feature. Broad units such as horst and graben belong to the opposite end of the scale spectrum (regional). The distribution of scales is fractal and their superposition creates a complex of features with spatial characteristics that may vary considerably with respect to location. Thus, while some long(er) wavelength features are more or less easily discernible, the short(er) wavelength lineaments are not. From the analyst's point of view things are worse when the topographic or magnetic landscape is controlled by the superposition of complex, past and contemporary tectonic modes. Fault scarps and fault zones are relatively long and narrow and can easily be distorted by interlacing with neighbouring sub-parallel or transverse features and buried in the long wavelength topographic or magnetic background. As a result, their position and effects on the landscape (lineaments) are not always straightforward to observe. The interfering landscape elements and scales must be separated or removed, a feat feasible with edge detection and spatial filtering methods of analysis.

The most frequently used edge detection methods (gradient directional filters, embossing filters, differential filters) in combination with directional illumination are usually effective in determining *local* gradient changes, even in complex landscapes. However, they cannot process and isolate the scale of changes, neither decompose the available information into components with particular spatial characteristics, which would facilitate scrutiny and appraisal of their relative importance. Yet, such facilities would be very welcome tools when trying to make sense out of very complex landscapes, as in the study area.

When faced with such problems, one must turn to less known but more effective methods of analysis. Herein we use bidirectional differentiation, two-dimensional wavelet imaging and two-dimensional K-space (wavenumber) filtering, adapted from the F-K filtering methods of petroleum geophysics. These are duly presented in Section 3. To the best of our knowledge, some of these techniques (for instance K-space filtering) have not been hitherto applied to the analysis of landscapes, but are shown to be very powerful and effective tools.

2. Geology and tectonics

The area of central-eastern mainland Greece (Fig. 1) is underlain by extensive formations of iron-rich (magnetic) rocks. Specifically, these comprise: (a) the ultramafic and volcanic components of the ophiolite complex in Mts Kallidromon and Knimis and the "schist-chert formation" to the south of Mt Chlomon; (b) the volcanic and iron-enriched components of the Permo-Triassic volcano-sedimentary complex at the base of the Sub-Pelagonian platform (south of Atalanti and in the area of Melidoni); (c) the quaternary volcanics of the northern Gulf of Evia (at Lichades, Agios Konstantinos and Kamena Vourla).

Moreover, this is a tectonically active and unusually intricate realm, apparently hosting a number of different faults, faulting zones and tectogenic structures that forge the topography, and leave diverse, frequently intense and occasionally impressive imprints on the terrain. In a nutshell, the tectonic fabric of our study area comprises (Fig. 1):

- *Major, range-bounding E–W to ESE–WNW faults and fault zones*: These are the best-known structures that control the succession of horsts and graben in the area, such as the North Gulf of Evia, the Lokris and the Voiotikos Kifissos basins. Representative structures of this category are the Atalanti fault zone, the Arkitsa–Agios Konstantinos–Kamena Vourla coastal fault system

and the Kallidromon fault zone in the mainland Greece and the Telethrion and Kandilion faults, which mark the north-eastern margin of the North Gulf of Evia.

The western part of the southern margin of the North Gulf of Evia is largely controlled by the Arkitsa–Agios Konstantinos–Kamena Vourla fault system, which comprises three fault zones: two of them, the eastern and western ones (Arkitsa-Longos (AF) and Kamena Vourla (KVF) fault zones, respectively) strike E–W and consist of fault segments with lengths from 3 to 8 km, arranged en echelon or relay. These two fault zones are linked by the NW–SE Agios Konstantinos fault (AKF). The reason why we did not consider these three structures to be a single fault zone is that, although they have common kinematic characteristics, their geometry is clearly different: the slip vectors measured on the fresh slickensides of all three are almost invariably oriented N–NNW (340–360°—Kranis, 1999), but the strike and dip of the fault planes differ significantly in the NW–SE Agios Konstantinos fault, whose fault surface has quite low dip values (∼30). To the west of this fault system extends the Molos fault zone, which comprises two overlapping, right-stepping ESE–WNW segments; this is quite less pronounced because it develops on the soft Neogene sediments of the Lokris basin.

The only fault zone along the southern margin of the North Gulf of Evia related to important recent earthquake events is the Atalanti fault zone (Ata), which strikes ESE–WNW and consists of three segments (Ganas et al., 1998; Palyvos, 2001; Pantosti et al., 2001). The total length of the Atalanti FZ is ∼35 km. There have been no reports on direct measurements of kinematic indicators, however, Skuphos (1894) reported that the superficial breaks of the 1894 earthquakes included a left-lateral component.

The northern margin of the Gulf is controlled mainly by two fault zones, the Telethrion and Kandilion faults, a large part of which develops offshore; hence the absence of first-hand data on their geometry and kinematics. The relationship between these two structures is currently a matter of investigation.

The Kallidromon fault zone (Kal) is a ∼33-km long structure and consists of two segments. It apparently is less active that the coastal fault zones (Jackson, 1999; Kranis, 1999). The kinematics of this fault is not as well defined, as in the aforementioned structures. Nevertheless, Kranis (1999) indicated that it is also oblique-normal, but with opposite shear sense (right-lateral strike-slip component). Another conspicuous structure is the Parnassos fault, which is a reactivated alpine thrust surface, having acted until at least the middle Quaternary as a low-angle normal fault (Kranis and Papanikolaou, 2001).

A second set of recognizable (and mapable) structures are NE–SW transverse faults and fault zones, located at the tips of, or within transfer zones, between the E–W neotectonic structures. The most prominent cases are the following:

(i) The Bralos-Oiti or Bralos-Pavliani fault zone (BrOe), located between Mts Kallidromon and Oiti, at the onshore SW-prolongation of the Oreoi straits. The lithology in the area does not favour direct field observations, as the fault zone crosses mud-rich flysch. Nonetheless, there are some isolated fault exposures, as in the case of the Skamnos segment which has a ENE–WSW strike and bears striations that indicate oblique sinistral offset. Moreover, the drainage pattern of the Assopos river, which develops along the trace of this zone, indicates strong tectonic influence through NE–SW zones (Kranis, 1999, 2002). This fault zone can also be associated with the 1983 six-month earthquake swarm located in the vicinity of Pavliani (Burton et al., 1995; Kranis, 2002).
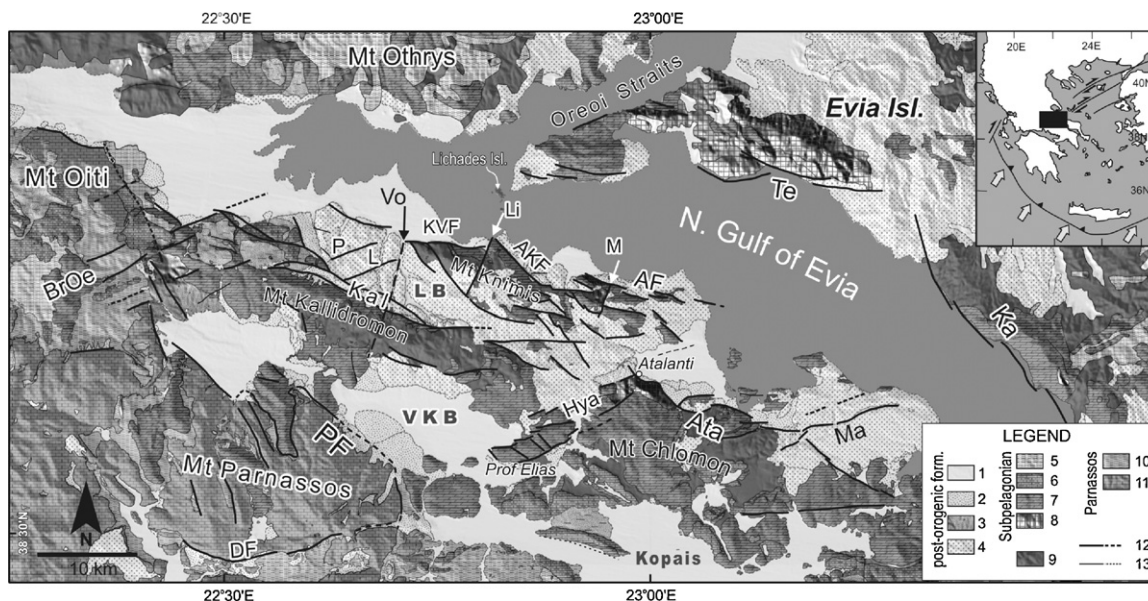
Fig. 1. Simplified geological and tectonic map of the study area, with the faults (F) and fault zones (FZ) referenced in text. 1: alluvium; 2: quaternary scree; 3: Bralos formation (Pleistocene); 4: Fluvio-lacustrine deposits (Pliocene-Earty Quaternary); 5: Late Cretaceous Clastics; 6: Late Cretaceous carbonates; 7: Triassic-Jurasic carbonates; 8: volcaniclastic complex and Sub-Pelagonian basement; 9: ophiolite suite; 10: Parnassos Unit flysch; 11: P.U. carbonates; 12: major faults; 13: minor faults. Te: Telethrion FZ; Kandilion FZ; Ma: Malesina FZ; Ata: Atalanti FZ; Hya: Hyampolis FZ; AF: Arkitsa FZ; AKF: Agios Konstantinos FZ; KVF: Kamena Vourla FZ; BrOe: Bralos-Oiti FZ; Ka: Kallidromon FZ; P: Potamia F; L: Liapatorrema F; Li: Lihades F; M: Melidoni F; Vo: Voagrios F; LB: Lokris basin; VKB: Voiotikos Kifissos basin.

(ii) The Hyambolis (Hya) fault zone (Palyvos, 2001; Kranis et al., 2001): It has been mapped along the western and northwestern margins of Mt Chlomo and consists of E–W to ENE–WSW-trending left-stepping en echelon segments. The Profitis Elias Sfakas horst, located at the SW portion of the zone is a prominent feature of the deformation zone (located along a restraining bend of it) and is clearly discernible in all topographic and aeromagnetic analyses performed within the scope of this study. This structure seems to play an important role, acting as a barrier (albeit not clearly active) on the western tip of the ESE–WNW Atalanti fault zone, which does not extend further west, into the Lokris basin.

(iii) The Malesina (Ma) fault zone: this active structure (it ruptured in the 1894 earthquakes, see Pantosti et al., 2001 for discussion) has an overall NE–SW trend, is linked with the Atalanti fault zone (and most probably affects its segmentation) and controls the morphology of the Malesina peninsula. However, unlike the previous two NE–SW fault zones, which can be characterized as oblique-slip, this one is more typical of a normal fault, with characteristic footwall back-tilt (Palyvos, 2001), although no directly measured kinematic indicators have been reported.

The third set of recognizable structures, are NNE–SSW (N10–20°) lineations mapped by Kranis (1999). They are found to cross the elongated ranges of Mts Knimis and Kallidromon, but, with the exception of the strike-slip Melidoni fault (MF) at eastern Knimis, no kinematic indicators have been found, nor has their activity been confirmed. A characteristic example is the Lihades fault (Li), which straddles Mt Knimis and seems to have facilitated the intrusion of the Lihades and Agios Konstantinos Upper Quaternary volcanics. Another one, found a few km west of it, is the Voagrios structure (Vo), which dissects Mt Kallidromon in two. Kranis (1999) noted that there are two major lineations that straddle the entire central-eastern mainland Greece (the Lihades–Antikyra and the Molos–Itea lineaments), the nature of which remains unclear.

3. Data analysis

The topographic and aeromagnetic data used in this study comprise a digital elevation model (DEM) and digital aeromagnetic anomaly model (DAAM).

The DEM is shown in Fig. 2a and was constructed from high resolution scanned images of the 1:50,000 scale topographic maps, compiled by the Hellenic Army Geographical Survey (HAGS). The images were digitized along contour lines and the digitized coordinates were transformed to the Hellenic Geographical Reference System (HGRS-87). The total field DAAM is shown in Fig. 2b and was created by digitizing the 1:50,000 residual anomaly aeromagnetic contour maps obtained from the Institute of Geological and Mining Research (IGME) and originally compiled by Hunting Geology and Geophysics Ltd. These maps were originally prepared so as to comply with the existing HAGS sheets. They were also digitized along contour lines and transformed to the HGRS-87. The Hunting maps were measured at a nominal flight altitude of 300 m a.g.l., with measurement spacing along flight lines ≤250 m and mean distance between flight lines ≈800 m. This affords a resolution of 250 m at best. Accordingly, we have interpolated the digitized contours onto a 250 m × 250 m HGRS-87 grid. The adopted digitization procedure allows a resolution as fine as the nominal error in the horizontal direction. For the elevation data this is as small as ±10 m and much finer than the resolution afforded for the aeromagnetic data. In order to maintain a healthy tradeoff between data volume and desired resolution while still being able to compare the results, the DEM was constructed by interpolating the digitized contours onto a HGRS-87 grid with 100 m × 100 m spacing.

The topography of the study area (and to a lesser extent the total magnetic intensity) exhibits a wide range of fractally distributed scales, from small hills and individual fault scarps to broad topographic units such as the horst and graben structures of the Kallidromon and Oiti mountain chains on the mainland and the Gulf of Evia, respectively. Since more than one contemporary faulting directions are known to exist (and more have existed in the past), the spectrum and interference of the different topographic scales create a complex pattern (noise) that may obscure many important
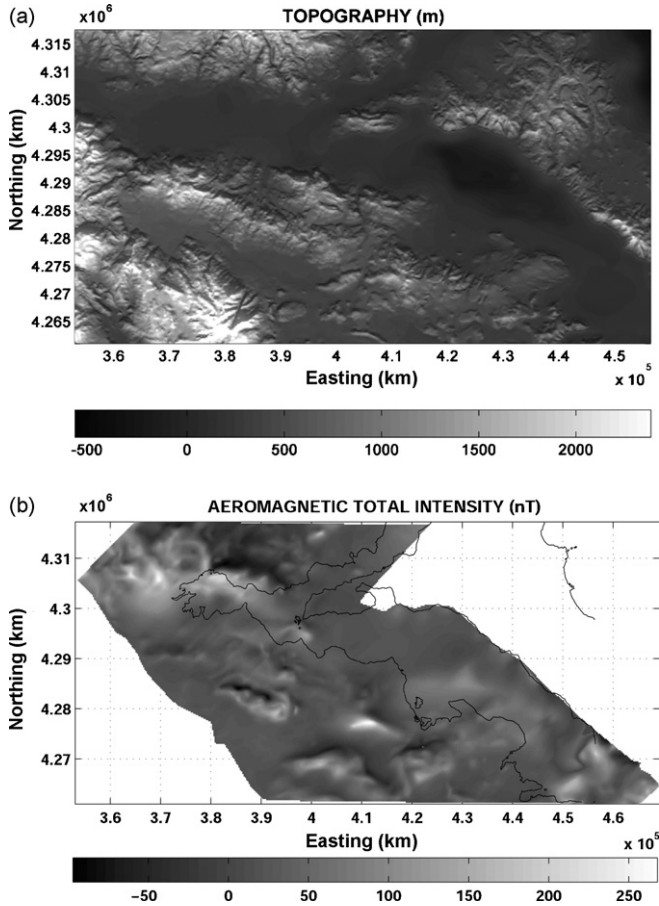
Fig. 2. (a) The digital elevation model of the study area (100 m grid spacing). (b) The digital aeromagnetic anomaly model of the study area.

linear features produced by the tectonic activity. Thus, while some long(er) wavelength features (e.g. small horsts and graben such as is the Profitis Elias Sfakas horst) are more or less easily discernible, the short(er) wavelength lineaments are not. We attempt to remove the interference and bring out the important linear features using the methods of analysis described forthwith.

3.1. Spatial differentiation

One robust and almost always dependable edge detection method is spatial differentiation, which eliminates long wavelength, slowly varying elements and enhances local, short wavelength changes, such as for instance fault scarps. Herein, we use double partial differentiation in mutually orthogonal directions. In operational form this can be written as

$$D_{xy}T = \frac{\partial}{\partial y}\left(\frac{\partial T}{\partial x}\right), \qquad (1)$$

where (x) is the equatorial and (y) is the meridional direction (or vice versa), and where T represents the DEM. The result of this operation (equivalent to a second order derivative) will show the spatial structure of the lateral rate of change in the topography, which according to the above discussion may indicate the position, orientation and size of faulting structures and lateral discontinuities. Moreover, it will attenuate trends almost exactly parallel to the (x) and (y) axes, thus eliminating clutter from linear elements with N–S and E–W orientations. This is a not undesirable side-effect, since our main objective is to study the NE–SW and NW–SE lineaments related to contemporary tectonics. It is also noted that such a

sequence of differentiations may produce random noise at an angle of 45° to suppress this effect the data is smoothed by convolving it with a diagonal 3-point Hamming filter.

3.2. Wavelet imaging

Edge detection can also be done with wavelet transformation (imaging), in combination with multi-scale analysis of the data. The wavelet transform can decompose a spatial data series into a spectrum of energy levels at given wavelength bands and given locations. In effect, the wavelet transform matches the spatial localization of the data to the wavelength of interest, providing fine resolution at short wavelengths and broad spatial localization at long wavelengths. This is much more versatile and informative than the Fourier transform, which will provide the power spectrum at given wavelength bands but for the *entire* data series, smoothing out any wavelength-local characteristics. On a single scale the wavelet transform is a linear, narrow-band filter. For multi-scale analysis the wavelet can be rescaled to longer and shorter lengths, providing a suite of different size filters, which are convolved with the data to pick out features with wavelengths matching the filters' bandwidths: small-scale events will match small wavelets but not large wavelets and vice versa. By applying the suite of filters to the spatial data it is possible to identify local (transient) characteristics, as well as distinguish features on different scales (or even identify regions where events of certain scales are missing).

Suitable wavelets for the stated purposes (edge detection and multi-scale analysis) are linear B-spline wavelets (Chui, 1992; Daubechies, 1992; Little et al., 1993; Little, 1994) and the derivative of the cubic B-spline (Canny, 1986; Little, 1994). Details on B-spline wavelets can be found in Chui (1992) or Daubechies (1992) and only essential information will be given herein.

The one-dimensional linear B-spline wavelet is constructed from the linear B-spline function.

$$N_2(x) = \begin{cases} 0 & x < 0 \\ x & 0 \le x < 1 \\ 2 - x & 1 \le x < 2 \\ 0 & x \ge 2 \end{cases} \qquad (2)$$

as

$$W_2 = \frac{1}{12}[N_2(2x) - 6N_2(2x - 1) + 10N_2(2x - 2) \\ - 6N_2(2x - 3) + N_2(2x - 4)] \qquad (3)$$

This wavelet transforms a step edge (change of slope) of scale comparable to the length of the wavelet, into a low and a high thus generating a series of contrasting peaks and valleys that demarcate local topographic changes.

In order to demonstrate how this wavelet transforms our data and provide a measure of the information to be mined with this approach, we present an example of its application on a single topographic profile running along a SSW–NNE direction at the west side of the study area, across the northern flanks of Mt Parnassos and through the Bralos plateau, Mt Kallidromon and the delta of Spercheios River to the southern foothills of Mt Othrys. This series of mountains and plateaus/valleys correspond to a series of horsts and graben formed by fault zones with very large cumulative vertical displacements and an average NW–SE orientation.

Fig. 3a shows the application of 20-point (middle panel) and 40-point (bottom panel) linear B-spline wavelets on the topographic profile (top panel). The 20-point wavelet will pick out features with widths (wavelengths) of the order of 2 km, comparable to its length,
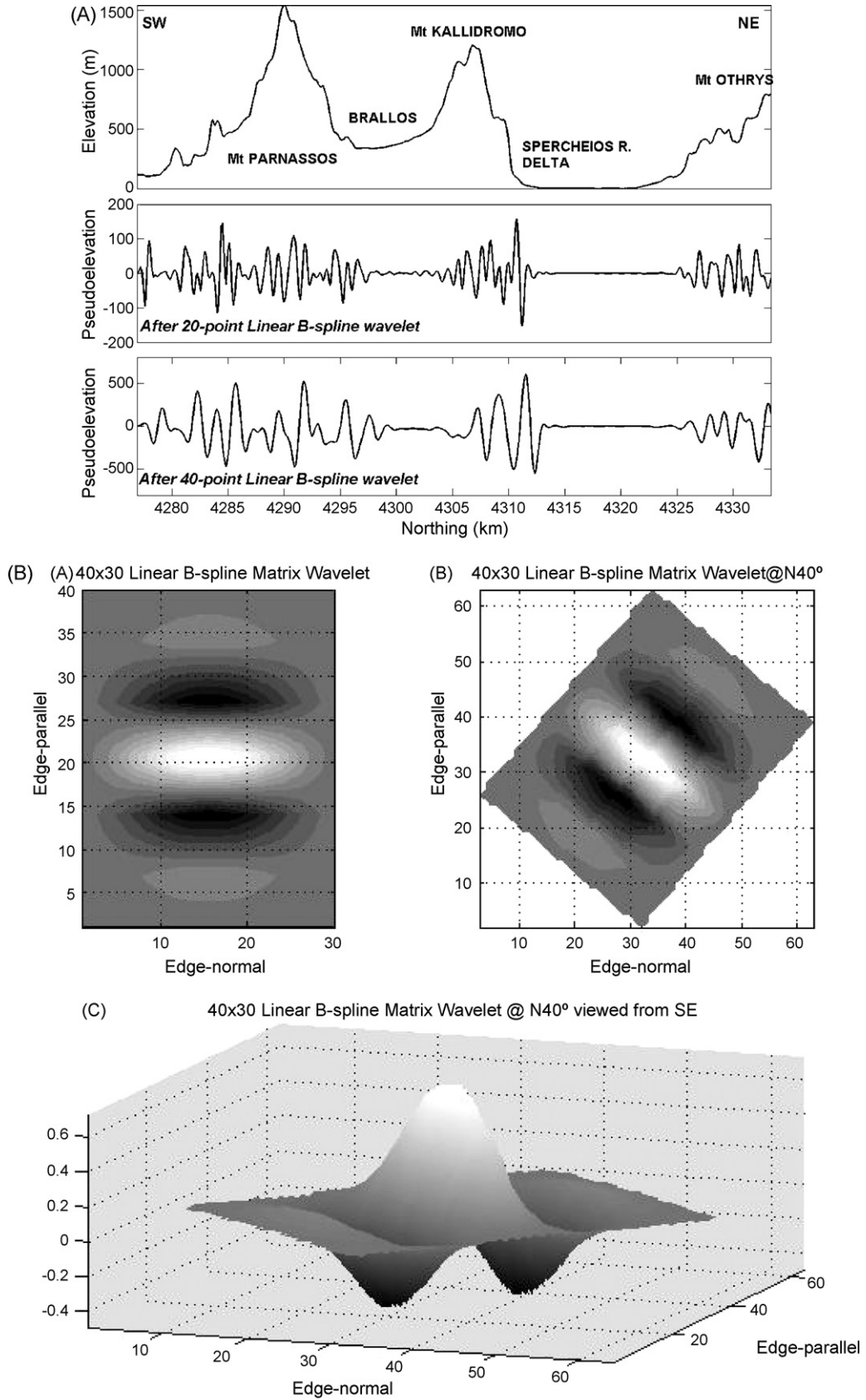
Fig. 3. (a) Application of 20-point (middle panel) and 40-point (bottom panel) linear B-spline wavelets on an elevation profile (top panel). (b) Top left: a 40 × 30 matrix filter of linear B-spline wavelets arranged in the S–N direction. To right: the same filter rotated to N40°. Bottom: three-dimensional view of the matrix filter shown in the top right panel.

while eliminating longer or shorter components. The topography is transformed into a series of highs and lows demarcating the locations of steps or breaks and, to the extent that these steps and breaks are produced by faults, the location of the faults. The 40-point wavelet will pick out features with widths of the order of 4 km, thus providing information on topographic steps and breaks of twice the width above (lower panel). Therefore, (to the extent that they are produced by faulting), the peaks and troughs of the considerably smoother 40-point transform will correspond to broader, possibly quasi-regional fault zones, in contrast to the more localized events brought out by the 20-point transform.

When the data depend on two spatial dimensions, (a matrix or image), the wavelet transform decomposes it into a series of images, each of which contains information at a specific location, of features at a single scale (wavelength). Moreover, the existence of two independent variables allows each wavelength to be coupled with a particular orientation. Thus, scale and orientation can be varied so as to construct a matrix filter tuned for any trait in the topography. It follows that the precision in location (resolution) of any feature in the wavelet transform will depend on its scale. In our case, it will be a function of the width (primarily) and length of the lineament/fault zone.

The two-dimensional filter is built by sidewise arranging a number of identical one-dimensional wavelets to create a 2D matrix, tapering the edge-parallel direction with a Hanning window and rotating the resulting matrix to the desired orientation. The length of the one-dimensional wavelet (edge-normal direction) determines the width of the topographic features to be isolated. The number of parallel wavelets (edge-parallel direction) determines the feature length over which to smooth. If the edge-parallel size is large, then only very long and linear features will be identified. If it is small, then both long and short (or curved) features will be picked out. As an example, in Fig. 3b we present a 40×30 matrix filter of linear B-spline wavelets arranged in a S–N direction (top left), which will detect E–W edges with widths of the order of 4 km, smoothed over lengths of 3 km. The same filter rotated to N40° (top right and bottom) will detect features with similar scales and orientations N130° and N310°.

3.3. K-space filtering

The DEM was also processed with a two-dimensional K-space filter in order to isolate and study elements with different orientations. To the extent that topography is controlled by tectonics, the separation of oppositely oriented topographic features removes much of the clutter caused by their superposition and facilitates more clear observations of the effects of different tectonic modes on the topography, and their relative importance thereof. To this effect, we have implemented techniques of F-K domain filtering (borrowed from petroleum geophysics and applied to the two-dimensional Fourier transforms of matrices with one temporal and one spatial dimension), to the k_x–k_y domain resulting from the two-dimensional Fourier transformation of matrices with two spatial dimensions. A good introduction to F-K techniques exists in Robinson et al. (1986). It is quite straightforward, although beyond the scope of this paper, to show that features with positive slope (NE–SW oriented or up-dipping in geophysical jargon) map into the positive k_y quadrant of the k_x–k_y domain, while features with negative slope (NW–SE oriented or down-dipping) map into the negative k_y quadrant. Therefore, by specifying a filter that stops an entire quadrant while passing the other, we can reject features oriented in one direction or the other. Furthermore, in the wavenumber domain it is possible to define specific pass or stop regions such as to further isolate and process (attenuate or amplify) specific spatial sub-characters of the data. In this way we can separate intersecting or overlaid elements and study their interactions.

For instance, it is possible to see which lineaments are relatively younger or more active by studying their effect on lineaments with transverse orientations.

3.4. Edge detection in aeromagnetic data

There exist several edge detection methods with particular application to magnetic and aeromagnetic data. These include the horizontal gradient method and the application of some type of compass gradient filtering on the observed data grid, or on the horizontal gradient of the pseudogravity transform (Blakely and Simpson, 1986), or the total gradient (e.g. Phillips, 1998), or on the local wavenumber (e.g. Thurston and Smith, 1997). These methods are tuned to detect discontinuities and boundaries between magnetic–non-magnetic formations by determining the direction of maximum slope of first order derivatives, or linear combinations of first and second order derivatives (local wavenumber).

Some of these methods rely on drastic assumptions, or are very susceptible to noise. For example, the method by Blakely and Simpson (1986) requires vertical contacts between magnetic and non-magnetic formations (Grauch and Cordell, 1987), while the correct calculation of the pseudogravity transform calls for a quasi-homogeneous distribution of the total magnetization vector over the study area. Violation of these assumptions can result in displacement of the contacts away (typically down dip) from their true locations (Grauch and Cordell, 1987). Neither one of these conditions is satisfied for our data. The distribution of the total magnetization vector is both unknown and highly heterogeneous (see Section 2 for details), while the tectonic (Alpine) emplacement of the main magnetic formations and their continuous post-alpine disturbances do not guarantee the existence of upright contacts. The local wavenumber method implements cascaded partial differentiations, which introduce noise unless the data is smoothed or upward continued, in which case small amplitude features are lost.

The 3D analytic signal has been introduced by Nabighian (1984), who also showed by way of the generalized Hilbert transform, that the vertical and horizontal derivatives of a potential field are related as

$$F\left\{\frac{\partial M}{\partial z}\right\} = -\frac{ik_x}{\sqrt{k_x^2 + k_y^2}} F\left\{\frac{\partial M}{\partial x}\right\} - \frac{ik_y}{\sqrt{k_x^2 + k_y^2}} F\left\{\frac{\partial M}{\partial y}\right\} \tag{4}$$

where $F\{\bullet\}$ denotes the Fourier transform and M stands for the DAAM. The total gradient is, then,

$$G = \frac{\partial M}{\partial x}i + \frac{\partial M}{\partial y}j + \frac{\partial M}{\partial z}k \tag{5}$$

The modulus of the total gradient

$$A = \sqrt{\left(\frac{\partial M}{\partial x}\right)^2 + \left(\frac{\partial M}{\partial y}\right)^2 + \left(\frac{\partial M}{\partial z}\right)^2} \tag{6}$$

can be shown to peak over isolated magnetic contacts and can be used as an indicator of local changes in the DAAM (e.g. Roest et al., 1992). Because this method requires the computation of the vertical derivative by means of the Fourier transform of the horizontal derivatives, it may be somewhat more susceptible to noise than the Blakely and Simpson method. However, there is no reduction-to-the-pole transformation required (and no relevant distortion). Moreover, it is not subject to the same assumptions and does not result in displaced contacts. For all the above reasons, herein we will implement the analytic signal (total gradient) method.
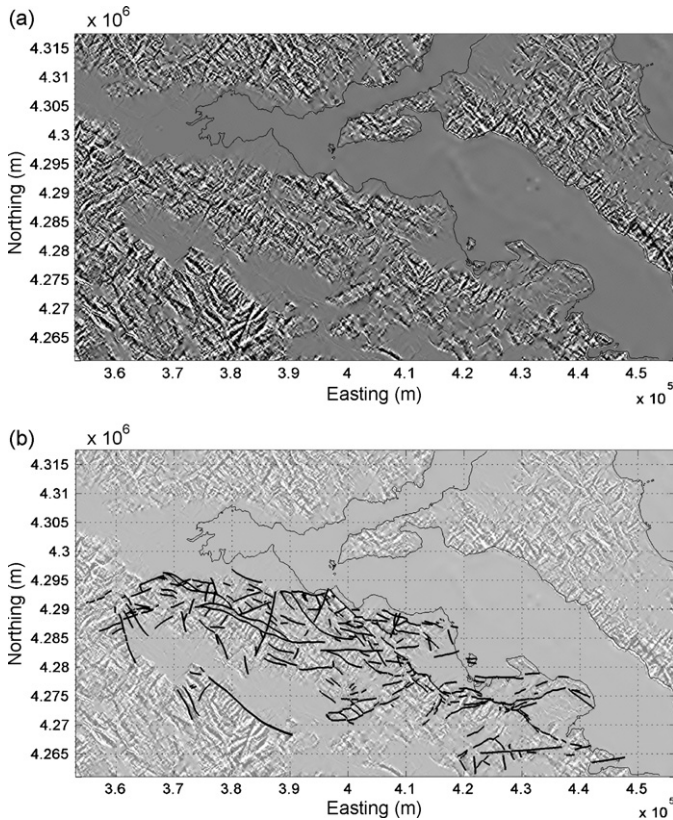
Fig. 4. (a) The gradient $D_{xy}T$ of the DEM calculated with Eq. (1). (b) The gradient $D_{xy}T$ of the DEM with the traces of active faults recognized by Kranis (1999) and Palyvos (2001).

4. Results and observations

4.1. Topographic lineaments and active faults

Fig. 4a presents the topographic gradient $D_{xy}T$ of the DEM and Fig. 4b is the same, but with inclusion of the traces of active neo-tectonic faults recognized by direct field observation: this is the most detailed image of *local* changes in topography, afforded by this data. The figure clearly illustrates the existence of significant lineaments with NNE–SSW, NE–SW and ESE–WNW orientations. The topographic gradient has higher amplitude at the location of significant topographic discontinuities, given also that the magnitude of a morphological discontinuity depends on the activity (deformation rate) of a faulting structure, its kinematics and the lithology: the more discernible combination is dip-slip or oblique-slip kinematics with a footwall comprising hard (erosion-resistant) rocks.

Very good correlation between ESE–WNW of lineaments and faults can readily be observed, as in the case of the Ata-lanti fault zone (Ata in Fig. 1), the extensive Kallidromon fault zone (Kal in Fig. 1), the Arkitsa–Agios Konstantinos–Kamena Vourla coastal fault system (AF–AKF–KVF in Fig. 1) and the Parnassos fault. All of the mapped range-bounding faults are typical neotectonic structures for the broader Aegean region (Stewart and Hancock, 1988). As stated in Section 1 their kinematics deviates significantly from pure dip-slip, by as much as 25% of strike-slip component. The coastal fault system is characterized by a systematic sinistral component, evidenced by the kinematic indicators on the exposed slickensides; the mean slip vector is N10°W and this value remains more or less constant, in spite of strike variations of the fault segments.

Likewise, there is very good correlation between ENE–WSW lineaments and ENE–WSW to NE–SW faults. One such significant example is the Bralos-Oiti (BrOe in Fig. 1). This lies in the SW-ward prolongation of the Oreoi Straits, a very narrow graben separating Evia from Magnesia and Fthiotis in mainland Greece. This structure is controlled by offshore NE–SW active faults (Perissoratis et al., 1991) and may well be related to propagation of the North Anatolian fault zone into the North Aegean (Sengör, 1979). Other important such structure with characteristic signature in the topographic gradient is the Hyampolis fault zone (Hya in Fig. 1). Located at the W and NW margin of Mt. Chlomo, it comprises a set of E–W to ENE–WSW left-stepping en echelon blocks (such as and the Profitis Elias Sfakas horst, Kranis et al., 2001), lending it a general NE–SW orientation. This structure intercepts the Atalanti fault zone and as stated in Section 1, may be responsible for the dramatic diminution of its cumulative vertical offset. A third important and seismically active NE–SW structure is the Malesina fault zone (Ma in Fig. 1); this may also affect the Atalanti fault zone, which it intercepts at the area of Martino. It is also possible to observe a SW-ward prolongation of the feature, which coincides with an ENE–WSW fault at the footwall of the Atalanti fault zone but with *opposite* polarity (dip). It is, thus, difficult to talk about a direct WSW extension of Malesina fault zone, across the footwall of the Atalanti fault zone. Even so, as seen in Fig. 4, these two fault zones appear to disrupt and discontinue the ESE–WNW normal faults.

Wavelet imaging was applied on the basis of the observations facilitated in Figs. 4 and 5a,b, respectively show the transforms resulting from a 20×20 matrix wavelet (resolution 2 km × 2 km) and a 40×40 matrix wavelet (resolution 4 km × 4 km), both oriented at N20° and roughly perpendicular to the dominant ESE–WNW lineaments of the topographic gradient. To increase
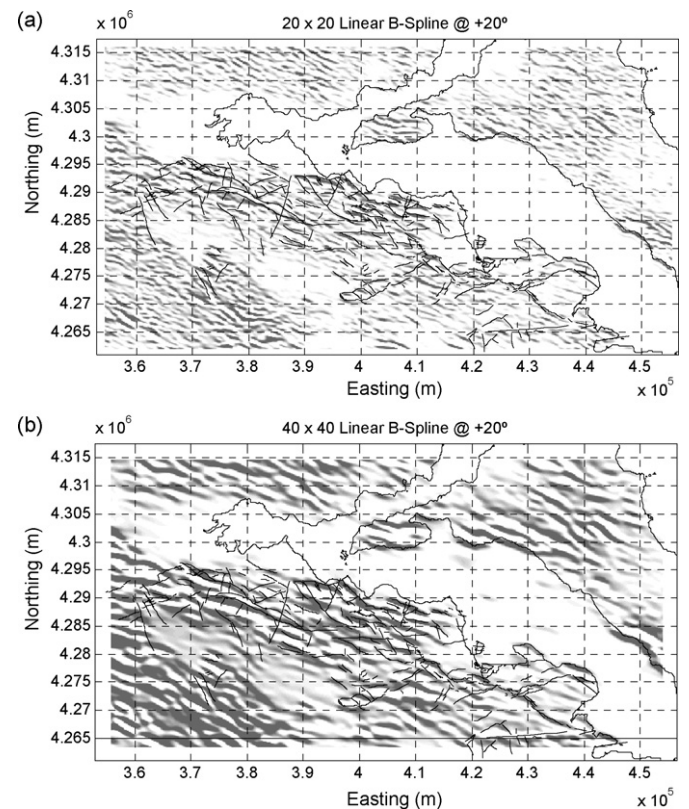

Fig. 5. (a) Image (wavelet transform) of the DEM using a 20×20 linear B-spline matrix wavelet oriented at N20°. (b) Image of the DEM using a 40×40 linear B-spline matrix wavelet oriented at N20°.

Fig. 6. (a) Image of the DEM using a 20 × 20 linear B-spline matrix wavelet oriented at N340°. (b) Image of the DEM using a 40 × 40 linear B-spline matrix wavelet oriented at N340°.
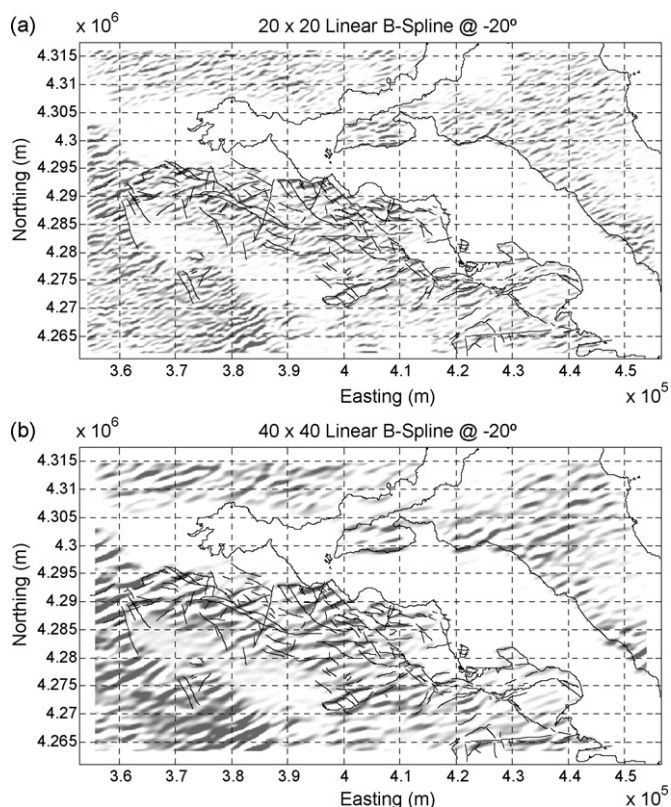
image readability, only the positive peaks of the wavelet transforms are shown. The existence of linear, coherent ESE–WNW changes in the terrain slope is immediately apparent. These correlate remarkably with the mapped traces of the range-bounding fault zones having corresponding orientation. Again, particular attention is drawn to the Ata, Kal, AF and Parnassos fault zones. The correlation between faults and topographic lineaments observed at the resolution level of grid spacing (Fig. 4) is shown to persist at increasingly larger scales. Accordingly, the fault zones producing these lineaments can be recognized as major landscape shaping factors. Additional, significant linear topographic changes can be observed in Fig. 5b, as SE-ward prolongations of the main inland and coastal fault zones. Since these are mainly observed at the larger scales, they may be associated with unmapped segments of the fault zones that cannot be easily detected by field surveys, possibly because their traces outcrop in softer rock and have been degraded by surface processes. Similar features can also be seen in the island of Evia and are believed to have been produced by corresponding tectonics.

Fig. 6a and b, respectively shows the transforms resulting from a 20 × 20 and a 40 × 40 matrix wavelets, both oriented at N340°, roughly perpendicular to the dominant ENE–WSW lineaments of the topographic gradient. Here as well, one can observe distinct NE–SW to ENE–WSW lineaments that correlate with mapped faults and fault zones, with particular reference to BrOe, Hya and Ma fault zones. Note however that the latter is more clearly observable at the larger scales. It is also apparent that the correlation persists at all scales, indicating that these fault zones are also very important in shaping the landscape.

All of the above fault zones are located at the margins of neotectonic structures. Nevertheless, we can still observe ENE–WSW faults within the neotectonic structures (neotectonic blocks). Such characteristic examples are the normal oblique-slip Potamia and

Liapatoremma faults (P and L in Fig. 1), which form a small horst within the west Lokris sub-basin (Mariolakos et al., 2001). These faults correlate well with ENE–WSW lineaments in Fig. 6a and b. Note however, that these lineaments are significantly longer than the mapped lengths of the faults, with particular reference to the Liapatoremma fault. This possibly implies the existence of faulting with a correspondingly significant scale, whose surface expressions may be obscured from field observations by the dense forest, and also by their interaction with transverse WNW–ESE and NNE–SSW structures (also see below).

Significant ENE–WSW lineaments can also be observed in Fig. 6a and b, approximately midway between the Liapatoremma/Potamia and Hyampolis fault zones, as well as in the island of Evia to the NE. In addition, very significant such topographic changes exist in the area of Mt Parnassos. In fact, these appear to be a natural extension/continuation of the Hyampolis (primarily) and Malesina fault zones, hinting to the existence of a long, broad and apparently important zone of faulting, disrupted only where it interacts with the transverse ESE–WNW fault systems. Such a zone would be expected to comprise a cardinal component of the contemporary tectonic evolution of central Greece.

A final observation concerns the existence of NNE–SSW faulting structures. Such elements were mapped by Kranis (1999), who could not observe clear evidence of their kinematics and present dynamic state, with the exception of the left-lateral strike-slip Melidoni fault zone (RM), which transverses the eastern portion of Mt Knimis, on the footwall of the Arkitsa fault.

Other characteristic examples of NNE–SSW structures are observed at larger scales (one order of magnitude higher). These are the Lichades fault zone (Li in Fig. 1), which transects Mts Knimis and Kallidromon and the Voagrios fault zone (Vo in Fig. 1) which transects Mt Kallidromon; notably, these lineaments appear to continue southwards and can be observed in the area of Mt Parnassos; Kranis (1999) has coined the names Lichades–Antikyra and Itea–Molos to these lineaments but did not interpret their origin and significance.

Finally, Fig. 7a and b shows the result of K-space dip-reject filtering on the DEM data. In Fig. 7a, which shows topographic elements with orientations in the 2nd and 4th quadrant (NW–SE), the dominant mode of topography is visible, comprising a sub-parallel series of ranges and basins, bounded by normal faults (among them Ar, Ata, Kal and Ma); wherever measured these show a non-trivial sinistral strike-slip component with NNW-oriented slip vectors. The Kallidromon–Chlomon and Parnassos ranges are readily discernible. The former becomes less clearly pronounced towards ESE; this lowering of footwall elevation was noted by Kranis (1999) for the Kallidromon range and was attributed by the same author to block rotation, caused by activity on presumed transverse faults. By comparing the results of K-space filtering of Fig. 7a with these of b, which shows topographic elements with orientations in the 1st and 3rd quadrant (NE–SW), it becomes clear that the transverse and/or oblique tectonic structures have played an important part in the tectonic configuration of the area. One can see that there are distinct "indentations" of the range fronts. This is apparently a secondary mode, comprising lower amplitude elements. One such example is at the intersection of the Ata with Hya, where the former terminates. The Voagrios discontinuity (Vo) also affects the western part of the Kallidromon mountain front. This is particularly visible in Fig. 7d. Another conspicuous feature is the abrupt western termination of Kallidromon range, which coincides with the Bralos-Oiti fault zone.

Furthermore, we extract elements with ENE–WSW (Fig. 7c) and NNE–SSW (Fig. 7d) orientations for further scrutiny. In Fig. 7c it becomes clear that the transverse structures with the largest amplitude and, consequently, importance are the BrOe and the Hya. These two may be the boundaries of a ∼35 km-wide deforming zone between the Sperchios graben and the Oreoi Straits in the north
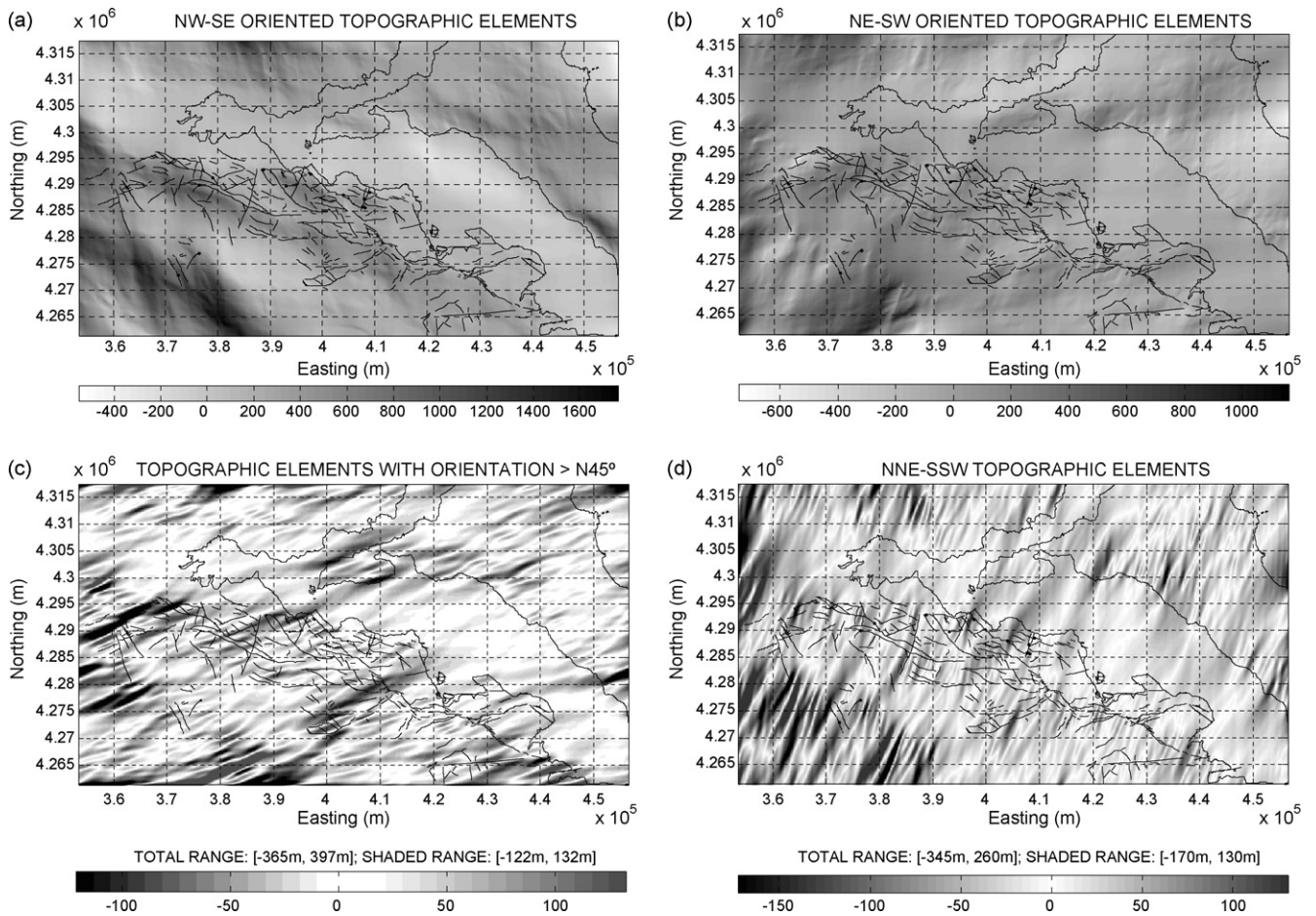
Fig. 7. (a) K-space filtered DEM in which only the NW–SE oriented topographic elements have been retained. (b) K-space filtered DEM in which only the NE–SW oriented topographic elements have been retained. (c) K-space filtered DEM illustrating topographic elements with exclusively ESE–WNW orientations. (d) K-space filtered DEM illustrating topographic elements with exclusively NNE–SWW orientations.

and the Malesina peninsula and Mt Chlomo in the south. Fig. 7d enhances some of the most elusive structures in the study area, including the Voagrios discontinuity. Another feature visible in the same figure lies approximately 10 km to the west of the Voagrios discontinuity and south of the Lichades Islets, crossing Mt Knimis. This structure has affected the segmentation of the coastal fault system and can be linked to the volcanic intrusions which have formed the islets and also outcrop a few km west of Kamena Vourla.

4.2. Aeromagnetic lineaments and active faults

Fig. 8a shows the amplitude $A > 0.01$ nT/m of the total gradient of the DAAM and Fig. 8b is the same but emphasizing the higher amplitude gradients ($A > 0.04$ nT/m). Fig. 9a and b, respectively shows the application of 8×8 linear B-spline matrix wavelets rotated to the direction N20° and N330°. Note that owing to the size of grid spacing (250 m), these filters will pick out scales of the order of $2 \text{ km} \times 2 \text{ km}$.

The gradient of the aeromagnetic data exhibits one family of significant NE–SW lineaments and one family of ESE–WNW lineaments. The major aeromagnetic and topographic lineaments are found to coincide and to have comparable scales with the topographic gradient lineaments, indicating that they are produced by significant discontinuities in the upper crust.

Specifically, very good correlation between ESE–WNW magnetic lineaments and neotectonic faults exists in the area of Atalanti fault zone (which transects Permo-Triassic formations and ophiolites in the area of Tragana) as well as in the areas of Knimis and Kallidromon fault zones, which are underlain by ophiolites with a particularly complex magnetic terrain. Additional evidence of such lineaments is also observed at Mt Othrys where ophiolites outcrop in abundance; these are evident in both Figs 8 and 9a and apparently correlate with topographic lineaments.

Strong correlations between ENE–WSW lineaments and faults are also observable in the area of Malesina fault zone and its likely prolongation across the footwall of Atalanti fault zone. To the south of Atalanti town, at the foothills of Mt Roda, the Permo-Triassic formations are characteristically bounded by faults parallel to the Atalanti fault zone and to the NE by the termination of the Hyampolis fault zone. The latter can also be traced at the area of Profitis Elias Sfakas (Fig. 1). The SE branch of the Hyampolis fault zone is correlated with a strong magnetic lineament and defines the boundary of the ophiolites (which are covered by post-alpine sediments). Evidence of ENE–WSW lineaments can be observed at the SE corner of the study area (apparently due to underwater sources), at the area of Lichades islands (presumably associated with the Quaternary volcanic activity of the area) and at Mt Othrys (ophiolites). Finally, weaker evidence of ENE–WSW lineaments exists at the ophiolitic complex of Mt Kallidromon.

4.3. Fault plane solutions and GPS velocity vectors and fault-slip data

Focal mechanism solutions of small to medium earthquakes can provide useful insights into the deformation pattern, especially in areas such as this, where deformation is distributed. Although
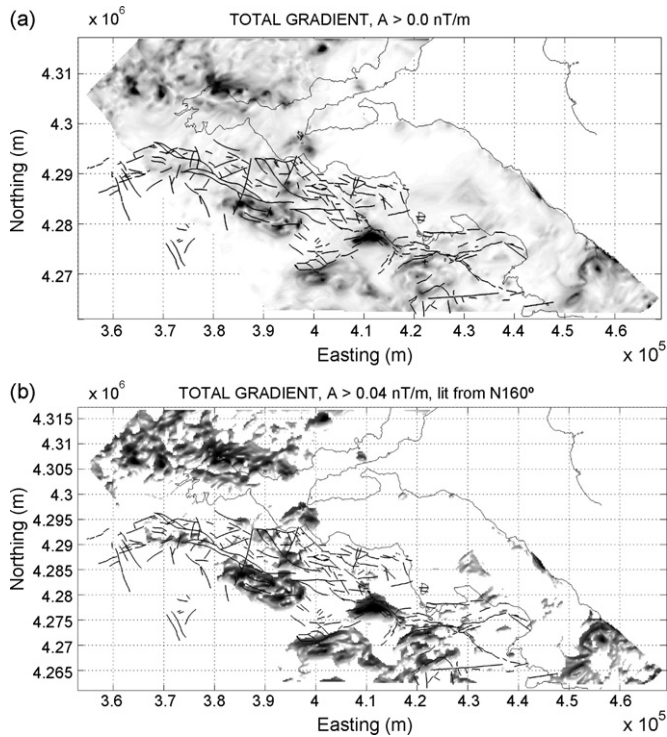
Fig. 8. (a) The total gradient A of the DAAM calculated with Eq. (6). (b) The total gradient A of the DAAM emphasizing the higher (*A* > 0.04 nT/m) values.

strain is primarily released by large events, a significant part could be released either aseismically, or by small earthquakes. These events account for a small amount of the total released strain but are helpful in bridging the strain rate deficit observed between strain rates calculated from earthquake data on one hand, and SLR and
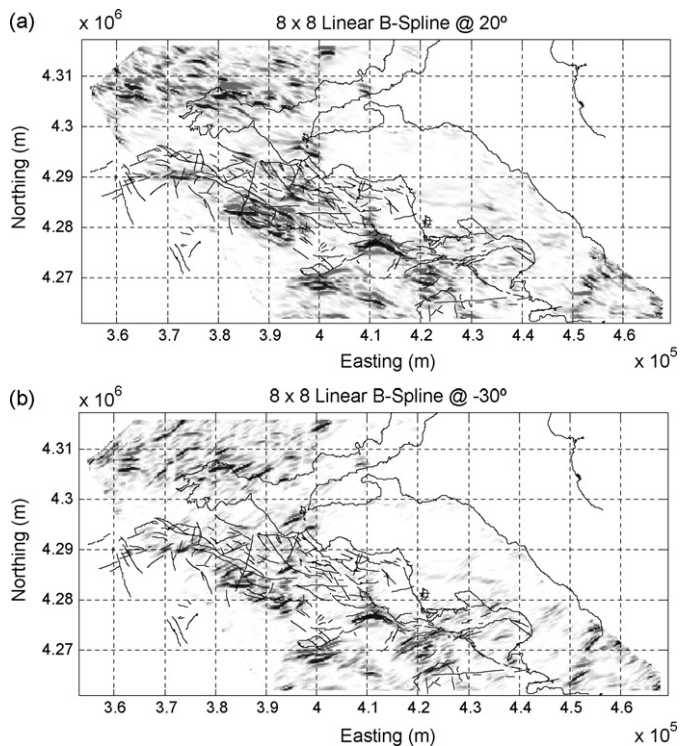

Fig. 9. (a) Image (wavelet transform) of the DAAM using an 8 × 8 linear B-spline matrix wavelet oriented at N20°. (b) Image of the DAAM using an 8 × 8 linear B-spline matrix wavelet oriented at N330°.
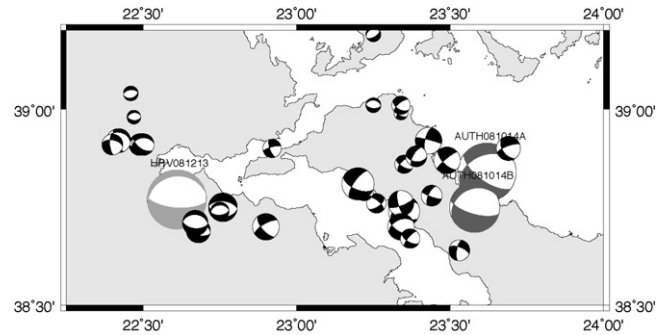

Fig. 10. Focal mechanisms of local earthquakes. The black beach balls indicate the small earthquake activity observed by local networks (Hatzfeld et al., 1999). The grey beach balls (AUTH) indicate the focal mechanisms computed by the University of Thessaloniki (Roumelioti et al., 2007). The light-grey beach balls (HRV) indicate the Harvard CMT mechanism of the 13/12/2008 event.

GPS data on the other (Jakcson et al., 1992; Clarke et al., 1998). Moreover, these data can be useful indicators as to the proposed re-adjustment of fault blocks (through rotation around vertical axes, Jackson, 2002) to accommodate the deformation imposed by the regional stress field.

Additional evidence on the dynamics and kinematics of the study area is presented in Figs. 10 and 11. Fig. 10 illustrates the focal mechanisms of small earthquakes observed by local networks and published by Hatzfeld et al. (1999). Superimposed are focal mechanisms of the main event ($M_W = 5.1$) and major aftershock ($M_W = 4.4$) of the 14/10/2008 Mantoudi earthquake sequence, computed by the University of Thessaloniki (Roumelioti et al., 2007), as well as the Harvard CMT mechanism of the 13/12/2008 $M_W = 5.2$ event. Fig. 11 displays the horizontal projections of the slip vectors of both nodal planes from the focal mechanisms of Hatzfeld et al. (1999), together with the GPS velocity vectors published by Clarke et al. (1998) and the mean fault-slip vectors computed herein.

The focal mechanism solutions show mostly oblique-slip motion, with one nodal plane striking NW–SE and one second nodal plane ENE–WSW. The slip vectors of the NW–SE nodal plane generally point to the SE and would appear to indicate that the area is moving to this direction, as is actually contended by Hatzfeld et al. (1999). The slip vectors of the ENE–WSW nodal planes would appear to indicate that the area is moving SW-ward, which is consistent with the GPS observations. Most importantly, the focal plane solutions indicate that the active tectonics of the study area include a NE–SW lateral component, which is parallel to the ENE–WSW
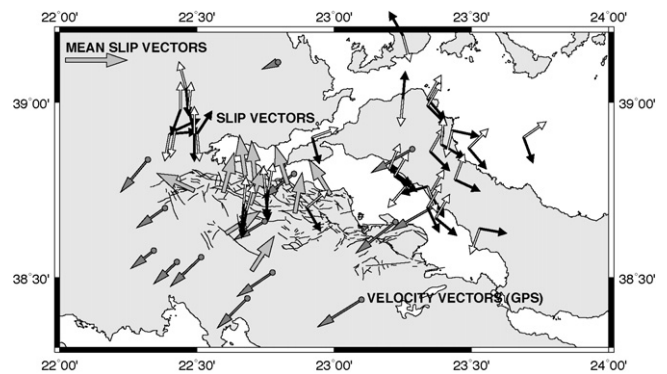

Fig. 11. The small black and white arrows indicate the horizontal projections of the slip vectors calculated from the focal mechanisms of Fig. 10 (Hatzfeld et al., 1999). The thin grey arrows indicate the GPS velocity vectors from Clarke et al. (1998). The thick grey arrows indicate the fault mean fault-slip vectors, for each of the fault segments described in text.
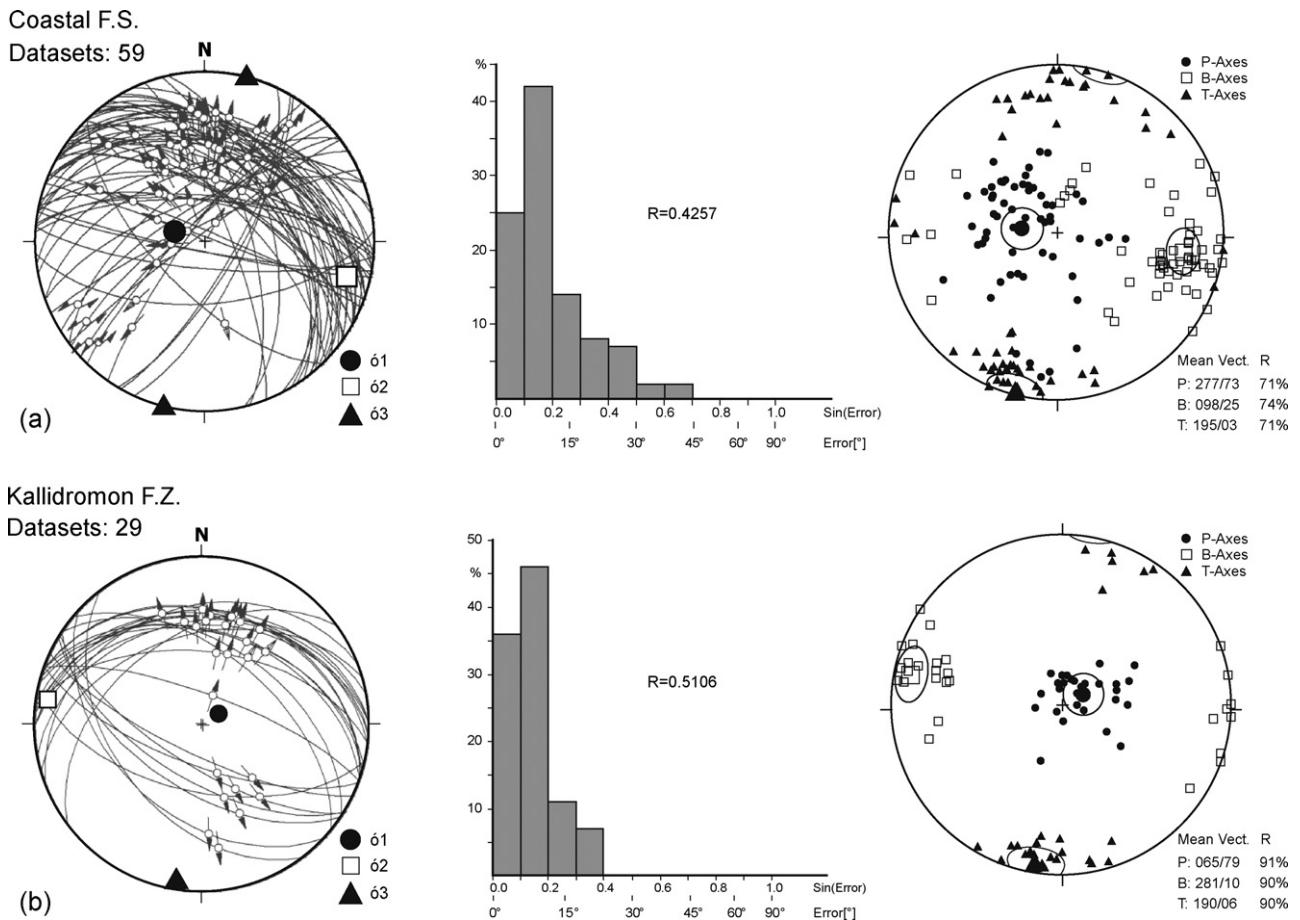
Fig. 12. Fault-slip data and calculation of stress tensor with the method of direct inversion for the coastal fault system (a) and the Kallidromon fault zone (b), following the method of Angelier and Coguel (1979), with the use of TectonicsFP computer program. Lower hemisphere, equal-area stereographic projections. Left panes show fault-slip data and the calculated stress axes ($\sigma_1, \sigma_2, \sigma_3$), middle panes are fluctuation-histograms of the deviation angles (angle between measured and calculated slip vectors) and stress ratio $R(\sigma_2 - \sigma_3)/(\sigma_1 - \sigma_3)$; right panes are P–T axes.

neotectonic faults and topographic/aeromagnetic lineaments and consistent with field observations of kinematic indicators on the ENE–WSW trending faults.

Inversion of fault-slip data was performed, following the direct stress inversion method of Angelier and Coguel (1979) and using the computer program Tectonics FP (Reiter and Acs, 2003). Examples of the results are shown in Fig. 12. Analysis of fault-slip data has shown that the coastal fault system is characterized by NNW-oriented mean slip vector (341°/51°), while the mean slip vector for the whole Kallidromon f.z. is NNE (028°/60°). The resolved stress tensors for the coastal fault system and Kal show that extension direction is practically identical for both σ_3 and the corresponding T axes are oriented NNE–SSW (Fig. 12) although the coastal shows greater deviation between measured and calculated extension directions; the latter may be indicative of multi-phase tectonics having affected the coastal fault system, a notion suggested by Kranis (2007). Kranis and Papanikolaou (2001) had calculated NE-oriented extension for the Parnassos fault, based on two measurement stations, close to Amfikleia. This extension direction is compatible with the orientation of the Pliocene-Lower Pleistocene extension suggested by Mercier et al. (1989), which in turn means that the Parn (Parnassos fault) has ceased to operate. However, this may not be the case, as recently collected fault-slip data from the entire Parnassos mountain front show indications of N–S to NNE–SSW extension, which is compatible with the current stress field (Kranis and Skourtsos, work in preparation).

5. Discussion and conclusions

The central-eastern mainland Greece is part of a broad deforming zone between the western tip of the North Anatolian fault (actually the North Aegean Basin) and the Kefalonia right-lateral fault in western Greece (see Burchfiel, 2004 and Kilias et al., 2008, for recent discussions). It comprises a suite of more or less typical rifts, such as the graben of the gulfs of Corinth and Northern Evia. Its relationship with the ongoing regional geodynamic processes is still a matter of investigation, as the exact mode of deformation has not yet been elucidated. In their recent paper, Kilias et al. (2008) suggest that the broader area is characterized by a combination of strike-slip and extensional deformation, within an underlapping extensional zone, between the North Anatolian and Kefalonia faults.

Our study has investigated the detectability of well-known faulting structures with transformations of digital aeromagnetic and topographic models. We have also tried to appraise the existence of structures not readily recognized in the field and to confirm the existence of transverse structures which had been detected by field surveys but with varying degrees of ambiguity, due to the nature of the syn-rift deposits or alpine clastics, which do not favour the preservation of fault-related structures (esp. fault surfaces and kinematic indicators) and the age-old modification of the terrain by agriculture.

We have found that, in addition to the well-known active E–W structures, there are others, transverse and/or oblique to them,

which participate in the deformation of central Greece. These are, primarily, NE–SW oblique to strike-slip fault zones located at the present-day transfer zones between the E–W structures. Second, there are also NNE–SSW strike-slip zones that are detected on scales that range from a few km to several tens of kilometers. The latter are more enigmatic; they could correspond to a set of secondary shears (P-shears), were we to adopt a transtensional NE–SW stress field for the broader area. However, neither their kinematics nor their activity has been confirmed, so this suggestion cannot be easily confirmed (or rejected for that matter). It is, after all, well known that even in zones with well-defined transtensional deformation pattern, the identification of a specific structure and its placing within the standard classification of shear zone components has certain limitations (Harding et al., 1985).

We believe that together with the well-known E–W to ESE–WNW major structures, the NE–SW ones shown in this study accommodate deformation which facilitates the rotation of elongated blocks (Jackson, 1994; Goldsworthy et al., 2002) within a broad shear zone that incorporates significant amount of strike-slip deformation. Given that the vast majority of kinematic indicators (fault striations, earthquake slip vectors,) deviate substantially from being pure dip-slip, together with the results of GPS surveying, it is reasonable to believe that the stress field in central-eastern mainland Greece is transtensional. As shown by Kahle et al. (2000) the rifting process in the North Gulf of Evia is controlled by a combination of normal and sinistral components which is in accordance with our observations.

As for the NE–SW structures, they need not be active, strictly speaking; however – and this has been demonstrated in the case of the Hyambolis fault zone – they may function as passive segment margins, controlling the segmentation of the E–W fault zones and/or facilitated the break-up of the elongated fault blocks into smaller-order ones, thus reducing their overall rigidity.

The additional constraints placed by the slip vectors of the focal mechanism solutions (Hatzfeld et al., 1999) and the velocity field, as it is known from GPS surveys (Clarke et al., 1998; Kahle et al., 2000; McClusky et al., 2000) come to support our suggestions for the existence and function of the NE–SW structures, as a clear SW-oriented movement of the area can be confirmed.

In conclusion, the study of the NE–SW structures has shown that they correspond to shear zones, either localized, or functioning at a larger (crustal) scale. The kinematics of the faults identified within these structures varies between oblique-slip and strike-slip. These faults affect Neogene to Late Quaternary deposits and have been responsible for the formation of transverse depressions and horsts. Judging from the study of the smaller-scale structures, the overall kinematics of these large-scale zones must be oblique-slip (Kranis et al., 2001). Certainly, these structures require further scrutiny at both small and large scales, before their role and contribution to the contemporary tectonics of Central Greece is unequivocally recognized. Nevertheless, they have been detected by diverse methodologies and have considerable extent, as they seem to straddle the entire central-eastern Greece and Evia. All their observed attributes suggest that they function so as to facilitate the accommodation of NE–SW shear and may thus be related to the propagation and diffusion of the North Anatolian and North Aegean fault systems into the Greek mainland.

References

Angelier, J., Coguel, J., 1979. Sur une methode simple de determination des axes principaux des contraintes pur un population des failles. C.R. Acad. Sci. Paris D 288, 307–310.

Blakely, R.J., Simpson, R.W., 1986. Approximating edges of source bodies from magnetic or gravity anomalies. Geophysics 51 (7), 1494–1498.

Burchfiel, B.C., 2004. New technology: new geological challenges. GSA Today 14 (2), 4–10.

Burton, P.W., Melis, N.S., Brooks, M., 1995. Coseismic crustal deformation on a fault zone defined by microseismicity in the Pavliani area, central Greece. Geophys. J. Int. 123, 16–40.

Canny, J., 1986. A computational approach to edge detection. IEEE Trans. Pattern Anal. Mach. Intell. 8 (6), 679–698.

Chui, C.K., 1992. An Introduction to Wavelets. Academic Press, New York.

Clarke, P.J., Davies, R.R., England, P.C., Parsons, B., Billiris, H., Paradissis, D., Veis, G., Cross, P.A., Denys, P.H., Ashkenazi, V., Bingley, R., Kahle, H.-G., Muller, M.-V., Briole, P., 1998. Crustal strain in central Greece from repeated GPS measurements in the interval 1989–1997. Geophys. J. Int. 135, 195–214.

Daubechies, I., 1992. Ten Lectures on Wavelets, CBMS Regional Conference Series in Applied Mathematics. SIAM, Philadelphia, PA, USA.

Ganas, A., Roberts, G.P., Memou, T., 1998. Segment boundaries, the 1894 ruptures and strain patterns along the Atalanti Fault, central Greece. J. Geodyn. 26, 461–486.

Goldsworthy, M., Jackson, J., Haines, J., 2002. The continuity of active fault systems in Greece. Geophys. J. Int. 148, 596–618.

Grauch, V.J.S., Cordell, L., 1987. Limitations on determining density or magnetic boundaries from the horizontal gradient of gravity or pseudogravity data. Geophysics 52 (1), 118–121.

Harding, T.P., Vierbuchen, R.C., Christie-Blick, N., 1985. Structural styles, plate-tectonic settings and hydrocarbon traps of divergent (transtensional) wrench faults. In: Biddle, K.T., Christie-Blick, N. (Eds.), Strike-Slip Deformation, Basin Formation and Sedimentation. Soc. Econ. Paleont. and Mineral., pp. 51–77.

Hatzfeld, D., Ziazia, M., Kementzetzidou, D., Hatzidimitriou, P., Panagiotopoulos, D., Makropoulos, K., Papadimitriou, P., Deschamps, A., 1999. Microseismicity and focal mechanisms at the western termination of the North Anatolian Fault, and their implications for continental tectonics. Geophys. J. Int. 137, 891–908.

Jackson, J.A., 1994. Active tectonics of the Aegean region. Ann. Rev. Earth Planet Sci. 22, 239–271.

Jackson, J.A., 1999. Fault death: a perspective from actively deforming regions. J. Struct. Geol. 21, 1003–1010.

Jackson, J.A., 2002. Using earthquakes for continental tectonic geology. Intern. Handbook of Earthquake and Engineering Seismology, vol. 81A. IASPEI, pp. 491–503.

Jakcson, J.A., Haines, A., Holt, W., 1992. The horizontal velocity field in the deforming Aegean Sea region determined from the moment tensor of earthquakes. J. Geophys. Res. 97, 17657–17684.

Kahle, H.-G., Cocard, M., Yannick, P., Geiger, A., Reilinger, R., Barka, A., Veis, G., 2000. GPS-derived strain field within the boundary of the Eurasian, African and Arabian Plates. J. Geophys. Res. 105, 23353–23370.

Kilias, A.A., Tranos, M.D., Papadimitriou, E.E., Karakostas, V.G., 2008. The recent crustal deformation of the Hellenic orogen in Central Greece; the Kremasta and Sperchios Fault Systems and their relationship with the adjacent large structural features. Z. dr. Ges. Geowiss. 159, 533–547.

Kranis, H.D., 1999. Neotectonic activity of fault zones in Lokris, central-eastern mainland Greece (Lokris), Ph.D. Thesis, GAIA, No. 10, Univ. of Athens, 234 pp.

Kranis, H.D., Papanikolaou, D.I., 2001. Evidence for detachment faulting on the NE Parnassos mountain front (central Greece). Bull. Geol. Soc. Greece XXXIV/1, 281–287.

Kranis, H.D., 2002. Kinematics of active faults in Lokris, central Greece—block rotation within a crustal-scale shear zone? In: Michalik, J., Simon, L., Vozar, J. (Eds.), Proc. XVII Congress of the Carpatho-Balkan Geol Ass. Geologica Carpathica 53, 157–159.

Kranis, H.D., Palyvos, N., Livaditis, G., Maroukian, H., 2001. The Hyambolis Zone: geomorphological and tectonic evidence of a transverse structure in Lokris (central Greece). Bull. Geol. Soc. Greece XXXIV/1, 251–257.

Kranis, H.D., 2007. Neotectonic basin evolution in central-eastern mainland Greece. Proc. 11th Intern. Congress, Athens, May 2007. Bull. Geol. Soc. Greece 40, 360–373.

Little, S.A., 1994. In: Foufoula-Georgiou, E., Kumar, P. (Eds.), Wavelet Analysis of Seafloor Bathymetry: An Example, in Wavelets in Geophysics. Academic Press, San Diego, pp. 167–182.

Little, S.A., Carter, P.H., Smith, D.K., 1993. Wavelet analysis of a bathymetric profile reveals anomalous crust. Geophys. Res. Lett. 20 (18), 1915–1918.

Mariolakos, I., Kranis, H., Maroukian, H., Fountoulis, I., 2001. Tectonically controlled drainage evolution in Lokris (Sterea Hellas). Bull. Geol. Soc. Greece XXXIV/1, 175–182 (in Greek).

McClusky, S.C., Balassanian, S., Barka, A., Demir, C., Ergintav, S., Georgiev, I., Gurkan, O., Hamburger, M., Hurst, K., Kahle, H., Kastens, K., Kekelidze, G., King, R., Kotzev, V., Lenk, O., Mahmoud, S., Mishin, A., Nadariya, M., Ouzounis, A., Paradissis, D., Peter, Y., Prilepin, M., Reilinger, R., Sanli, I., Seeger, H., Tealeb, A., Toksoz, M.N., Veis, G., 2000. Global positioning system constraints on plate kinematics and dynamics in the eastern Mediterranean and Caucasus. J. Geophys. Res. 105, 5695–5719.

Mercier, J.L., Sorel, D., Vergely, P., 1989. Extensional tectonic regimes in the Aegean basins during the Cenozoic. Basin Res. 2, 49–71.

Nabighian, M.N., 1984. Toward a three-dimensional automatic interpretation of potential field data via generalized Hilbert transforms: fundamental relations. Geophysics 40 (6), 780–786.

Palyvos, N., 2001. Geomorphological study of the broader Atalanti area (Fthiotis, Central Greece), Ph.D. Thesis, Univ. of Athens, Dep. of Geology, 233 pp. (in Greek).

Pantosti, D., De Martini, P.D., Papanastassiou, D., Palyvos, N., Lemeille, F., Stavrakakis, G., 2001. A reappraisal of the 1894 Atalanti earthquake surface ruptures, Central Greece. Bull. Seis. Soc. Am. 91 (4), 760–780.

Perissoratis, C., Angelopoulos, I., Mitropoulos, D., Michailidis, S., 1991. Surficial Sediment Map of the Aegean Sea floor (Scale 1:200,000): Pagasitikos Sheet (and Explanatory Text). I.G.M.E., Athens.

Phillips, J.D., 1998. Processing and Interpretation of Aeromagnetic Data for the Santa Cruz Basin—Patagonia Mountains Area, South-Central Arizona, U.S. Geological Survey, Open-File Report 02-98.

Reiter, F., Acs, P., 2003. TectonicsFP Software, http://www.tectonicsfp.com.

Robinson, E.A., Durrani, T.S., Peardon, L.G., 1986. Geophysical Signal Processing. Prentice Hall, London, p. 389–467.

Roest, W.R., Verhoef, J., Pilkington, M., 1992. Magnetic interpretation using the 3-D analytic signal. Geophysics 57 (1), 116–125.

Roumelioti, Z., Benetatos, Ch., Kiratzi, A., Dreger, D., 2007. Near-real time moment tensors for earthquakes in Greece provided by the Dept of Geophysics, Aristotle University of Thessaloniki (AUTH-solutions), Report submitted to the European Mediterranean Seismological Center (EMSC), http://emsc-csem.org.

Sengör, A.M., 1979. The North Anatolian fault: is age, offset and tectonic significance. J. Geol. Soc. Lond. 136, 269–282.

Skuphos, T., 1894. Zwei grossen Erdbeben in Lokris am 8/20 und 15/27 April, 1894. Zeitschrift Ges. Erdkunde zu Berlin 24, 409–474.

Stewart, S., Hancock, P.L., 1988. Normal fault zone evolution and fault scarp degradation in the Aegean region. Basin Res. 1, 139–153.

Thurston, J.B., Smith, R.S., 1997. Automatic conversion of magnetic data to depth, dip, and susceptibility contrast using the SPItm method. Geophysics 62 (3), 807–813.